SUPPORTING INFORMATION

Uncovering Selective and Active Ga Surface Sites in Gallia-Alumina Mixed-Oxide Propane Dehydrogenation Catalysts by Dynamic Nuclear Polarization Surface Enhanced NMR Spectroscopy

Pedro Castro-Fernández,† Monu Kaushik,§ Zhuoran Wang,§ Deni Mance,‡ Evgenia Kountoupi,† Elena Willinger,† Paula M. Abdala,† Christophe Copéret,‡ Anne Lesage,§,* Alexey Fedorov†,*, Christoph R. Müller†,*

†Department of Mechanical and Process Engineering, ETH Zürich, CH-8092 Zurich, Switzerland

§High-Field NMR Center of Lyon, CNRS, ENS Lyon, Université Lyon1, UMR 5082, F-69100 Villeurbanne, France

‡Department of Chemistry and Applied Biosciences, ETH Zürich, CH-8093 Zürich, Switzerland

Corresponding Authors

anne.lesage@ens-lyon.fr (Anne Lesage)

fedoroal@ethz.ch (Alexey Fedorov)

muelchri@ethz.ch (Christoph R. Müller)

Table of Contents

FIGURES

TABLES

Experimental

Materials. Gallia-alumina NPs were prepared following a general literature method.[1] Ga(acac)$_3$ and Al(acac)$_3$ (99.99+%, Strem chemicals) were mixed at nominal Ga:Al molar ratios of 1:6, 1:3, 3:1 and 1:0, and at a total scale of 2 grams, with 40 mL of oleylamine (≥98%, Sigma-Aldrich) and stirred for 1 h at 90 °C under dynamic vacuum (ca. 10^{-1} mbar). Then, the vacuum was replaced by a flow of N_2 and the reaction mixture was heated to 200 °C (3 °C min^{-1}) and held at this temperature for 7 h. The product solution was washed four times with 40 mL of an ethanol - toluene mixture (3:1 ratio, ≥99.8% and ≥99.5%, Sigma-Aldrich, respectively) and centrifuged at 6500 rpm between the washing cycles. The product gel was dissolved in toluene to form a colloidal solution (ca. 35 mg mL^{-1}, according to thermogravimetric analysis). $(Ga,Al)_2O_3$ materials were prepared by drying the respective colloidal solutions at 100 °C for 12 h, followed by calcining the residue in a muffle furnace (650 °C, 2 h, 3 °C min^{-1}). γ-Al_2O_3 used was purchased from Alfa Aesar (99.9%, 40 µm mesh size, calcined at 700 °C for 2 h, S_{BET} = ca. 100 m^2 g^{-1}, V_{pore} = 0.26 mL g^{-1}). Pyridine (99.8%, Sigma-Aldrich), 2,6-dimethylpyridine (≥99%, Sigma Aldrich) and ^{15}N-labeled pyridine (98%, Cortecnet) were dried over CaH_2 (95%, Sigma-Aldrich) and degassed by three freeze−pump−thaw cycles. γ-Al_2O_3 was also used as a reference Ga-free catalyst.

X-Ray powder diffraction. XRD data were obtained using a Cu Kα radiation source (45 kV, 40 mA) in a PANalytical Empyrean diffractometer. An X'celerator Scientific ultra-fast line detector was used alongside Bragg-Brentano HD incident beam optics. XRD patterns were recorded between 2θ values of 20 and 90° (step size = 0.026 °; collection time = 0.8 s step^{-1}). The cubic cell parameter (*a*) was calculated using the d-spacing for the (440) plane obtained by fitting the corresponding peak and using the Bragg's law and eq 1.[2]

$$d_{hkl} = \frac{a_0}{\sqrt{h^2 + k^2 + l^2}} \qquad \text{(Eq. 1)}$$

X-Ray absorption spectroscopy. XAS experiments were performed at the BM31 station of the Swiss-Norwegian beamlines (SNBL) at the European Synchrotron Radiation Facility (ESRF).[3] Spectra were collected at the Ga K-edge in transmission mode and with continuous scanning. A double-crystal Si (111) monochromator was used. Materials were mixed with an optimal amount of cellulose and pressed into self-supporting pellets.[4] For data processing the Athena software was used (in the Demeter suite package).[5] The calibration energy was adjusted using a Zn-foil reference. The FEFF paths were generated with the Artemis program using a β-Ga_2O_3-based structure model that was also utilized to determine the amplitude reduction factor (S_0^2).[5,6]

Magic angle spinning nuclear magnetic resonance (MAS NMR). ^{27}Al and ^{71}Ga MAS NMR experiments were carried out in a Bruker Avance III 700 MHz spectrometer (16.4 T), using the Hahn-echo pulse sequence with an excitation pulse length of 1 µsec. Catalysts were loaded in 1.3 mm zirconia rotors protected with silicon caps spun at 50 kHz using nitrogen gas. All spectra were fitted using the DMFit software.[7,8]

^{15}N DNP SENS. Experiments were performed on a commercial Bruker Avance III 400 MHz wide bore spectrometer equipped with a Bruker 264 GHz gyrotron source for generating microwave (MW) irradiation. One-dimensional (1D) ^{15}N{^{1}H} cross polarization magic angle spinning (CPMAS), 1D ^{15}N{^{1}H} and ^{15}N{^{71}Ga} *J* coupling mediated heteronuclear multiple quantum correlation (*J*-HMQC) experiments were performed using a triple resonance 3.2 mm low-temperature MAS probe configured in the ^{1}H-^{27}Al-^{15}N or ^{1}H-^{71}Ga-^{15}N mode with the proper insert and shunt capacitor. The MW power was optimized such that the maximum DNP enhancement factor was obtained for each sample, where the DNP enhancement factor was determined by comparing the ^{1}H signal intensity with or without MW irradiation. The DNP build-up time constants were determined by fitting the polarization build-up curves obtained from ^{1}H saturation recovery experiments. More detailed experimental parameters are given in Table S10. The following parameter notation is used: ν_R denotes the MAS rate, ν_{RF}(^{1}H) and ν_{RF}(X) are the magnitudes of radio frequency (RF) magnetic fields applied to ^{1}H and X nuclei, τ_{CP} is the CP contact time (note that all CP experiments used ramped RF amplitude at the ^{1}H spin frequency), τ_{RD} is the recycle delay, *ns* is the number of scans, and *AT* is the total acquisition time. The ^{1}H, ^{15}N, ^{27}Al and ^{71}Ga chemical shift are referenced according to the IUPAC recommendations.

The ^{15}N labelled pyridine containing specimen were prepared by exposing dehydroxylated materials (500 °C, heating ramp 3 °C min^{-1}, ca. 10^{-5} mbar, 2 h) to the vapor of ^{15}N labelled pyridine at room temperature and desorbing pyridine at 100 °C. The materials were then transferred to a glovebox under an argon atmosphere (O_2 and H_2O levels were below 0.5 ppm). For DNP SENS experiments, the materials were impregnated with a 16 mM solution of TEKPol in 1,1,2,2-tetrachloroethane (TCE) and packed into 3.2 mm thin-wall zirconia rotors in the glovebox.

X-Ray photoelectron spectroscopy. XPS data was acquired on a Sigma II probe instrument (Thermo Fisher Scientific) with an ultra-high vacuum chamber and a non-monochromatic Al Kα source (200 W, hν = 1486.6 eV) in constant analyzer energy mode (CAE). A pass energy of 25 eV with a step size of 0.1 eV was used. Source and emission angles were set to 50º and 0º, respectively. All data processing was carried out using the Casa XPS software V. 2.3.19PR1.0. During data treatment, energy shift corrections were performed by adjusting the C 1s adventitious carbon peak to 284.8 eV. Background signals were subtracted using the Shirley algorithm,[9] while pseudo-Voigt line shapes were used for peak fitting.

Elemental analysis. Inductively coupled plasma–optical emission spectroscopy (ICP-OES) experiments were carried out on an Agilent 5100 VDV instrument calibrated utilizing a multi-element standard. The materials were dissolved in aqua regia (3:1; HCl:HNO_3) and kept at 175 ºC for 30 min in a microwave digestion system (Multiwave GO). The resulting solutions were diluted with deionized water to match the linear range of the standard.

N_2 physisorption. To determine the surface areas of the materials, N_2 physisorption was carried out in a Quantachrome NOVA 4000e instrument after degassing the materials at 200 °C for 2 h. The Brunauer-Emmett-Teller (BET) and Barrett-Joyner-Halenda (BJH) methods were used to determine the specific surface area and porosity, respectively.[10,11]

Pyridine adsorption FTIR. Prior to pyridine and 2,6-dimethylpyridine adsorption, self-supporting pellets were dehydroxylated at 500 ºC (3 ºC min^{-1}) for 2 h under ca. 10^{-5} mbar. The dehydroxylated materials were exposed to the pyridine vapor at room temperature for ca. 20 min. Subsequent outgassing was carried out at room temperature as well as at 100, 200 and 300 ºC, recording IR spectra after each evacuation step. Infrared spectra were obtained in transmission mode (resolution 4 cm^{-1}) using a Nicolet FTIR spectrometer with a DTGS detector (Thermo Fisher).

Catalytic tests. The performance in propane dehydrogenation was evaluated using a benchtop Microactivity EFFI reactor (PID Eng&Tech). A mixture of 50 mg of catalyst and 1.20 g of SiC (46 grit, Alfa-Aesar) was loaded between two plugs of quartz wool into a fixed-bed reactor containing a quartz frit as distributor (ø 13 mm). Nitrogen gas (30 ml min^{-1}) was flowed until the desired reaction temperature was reached (550 ºC, 10 ºC min^{-1}). Then, a mixture of 10% C_3H_8 in N_2 (WHSV = 7.2 h^{-1}) was flown into the reactor. The off-gas composition was analysed using a Clarus 480 gas chromatograph (Perkin-Elmer) equipped with a flame ionization detector (FID) and a thermal conductivity detector (TCD). The first chromatograms were acquired after 4 minutes and then every 20 minutes.

Thermogravimetric analysis. Thermogravimetric analyses were performed in a Mettler-Toledo DSC1 instrument. Ca. 15 mg of specimen was placed in a 70 µL alumina crucible and heated to 550 ºC (10 ºC min^{-1}) under a flow of 75 mL min^{-1} of N_2. The temperature was held at 550 ºC for 10 minutes and then a mixture of 10% C_3H_8 in N_2 was flown over the material. Changes in the specimen weight were monitored for 2 h.

Transmission Electron Microscopy (TEM). Colloidal solutions of nanoparticles were dispersed onto a copper grid and investigated using a FEI Tecnai F30 transmission electron microscope with a voltage of 300 kV equipped with a single tilt holder. Bandpass filters and contrast adjustments of the obtained images were applied using the ImageJ software.[12] The microstructure and electronic structure of the specimen were additionally investigated by analytical electron microscopy using a double Cs corrected (TEM&STEM) JEOL JEM-ARM300F Grand ARM scanning transmission electron microscope that was operated at 300 kV. The microscope is equipped with the Model 965 GIF Quantum ER EELS Spectrometer. For this TEM study, the calcined specimen were prepared by drop deposition of $(Ga,Al)_2O_3$ NPs dispersed in isopropanol onto a copper grid with a holey carbon support film. ADF-STEM images were recorded with a semi-convergence angle of 18 mrad and 33-106 mrad collection semi-angles. EELS spectra were recorded in STEM mode using a 2.5 mm entrance aperture, 50 meV dispersion and 1 µA emission current. The energy resolution obtained at these conditions was about 0.35 eV.

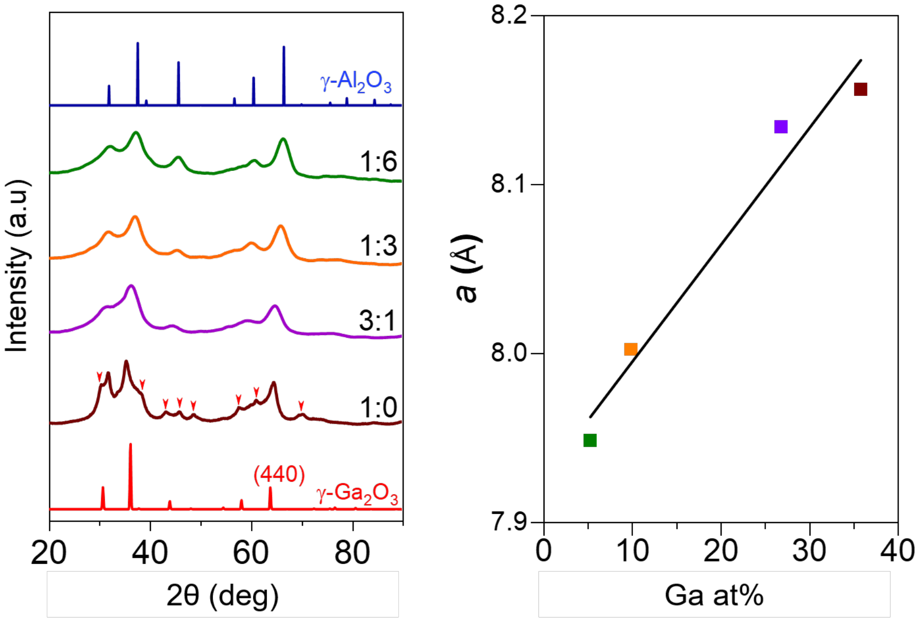

Figure S1. XRD patterns (left) of $(Ga,Al)_2O_{3(x:y)}$ NPs along with the references of γ-Ga_2O_3 (red) and γ-Al_2O_3 (blue).[13,14] Arrows in the trace of $(Ga,Al)_2O_{3(1:0)}$ indicate the peaks due to β-Ga_2O_3. Unit cell parameter (right), *a*, (based on the 2θ position of the (440) reflection) as a function of Ga atomic content in $(Ga,Al)_2O_{3(x:y)}$ materials.

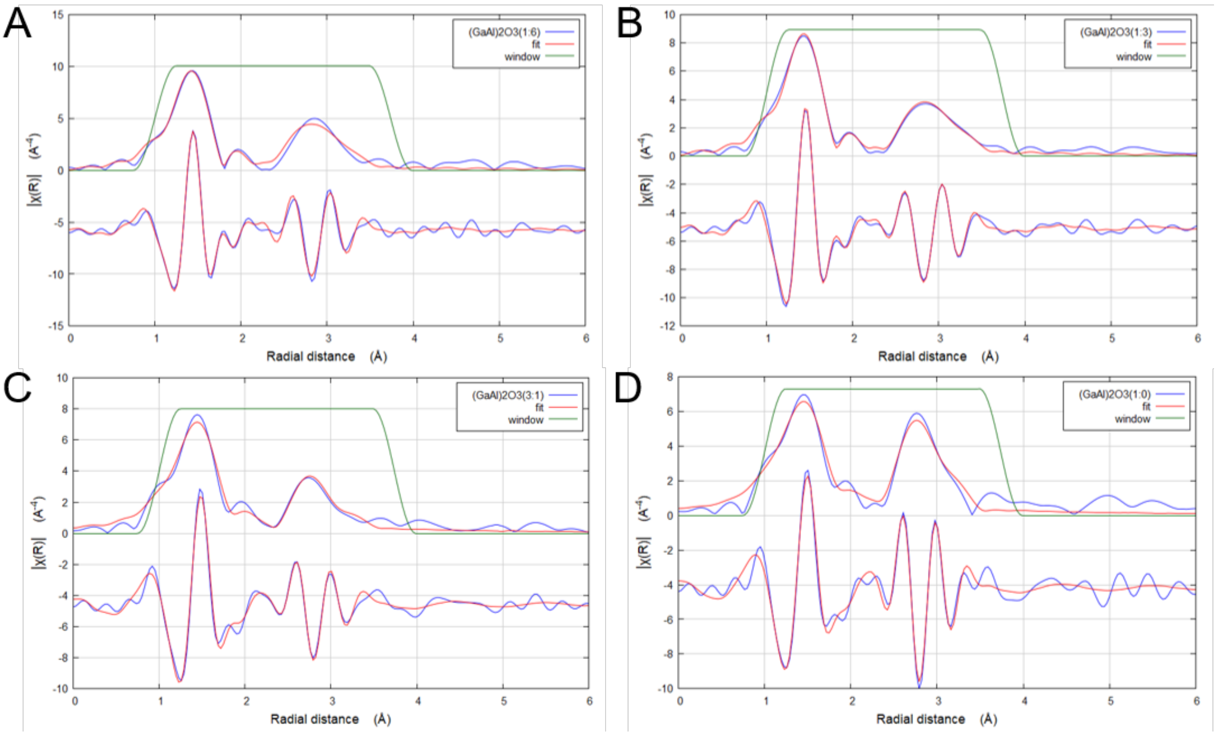

Figure S2. EXAFS fittings and experimental data of $(Ga,Al)_2O_3$ materials: (A) $(Ga,Al)_2O_{3(1:6)}$, (B) $(Ga,Al)_2O_{3(1:3)}$, (C) $(Ga,Al)_2O_{3(3:1)}$, (D) $(Ga,Al)_2O_{3(1:0)}$.

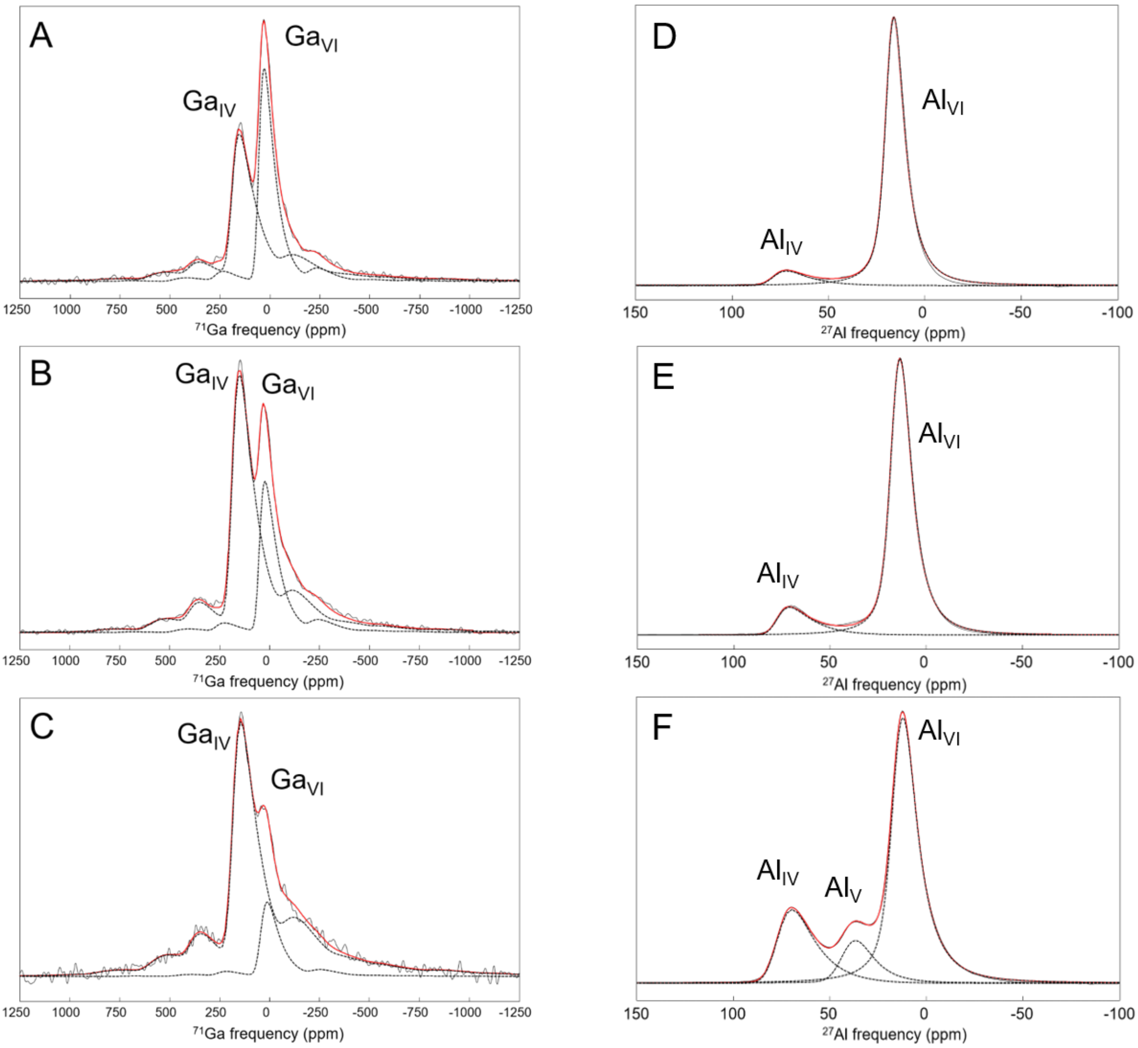

Figure S3. Fittings of ^{71}Ga and ^{27}Al MAS NMR spectra of $(Ga,Al)_2O_3$ materials. Panels (A) and (D) correspond to $(Ga,Al)_2O_{3(1:6)}$; (B) and (E) to $(Ga,Al)_2O_{3(1:3)}$; and (C) and (F) to $(Ga,Al)_2O_{3(3:1)}$. Captions indicate the corresponding coordination geometry for each peak. Results of these fittings are summarized in Tables S3-S4.

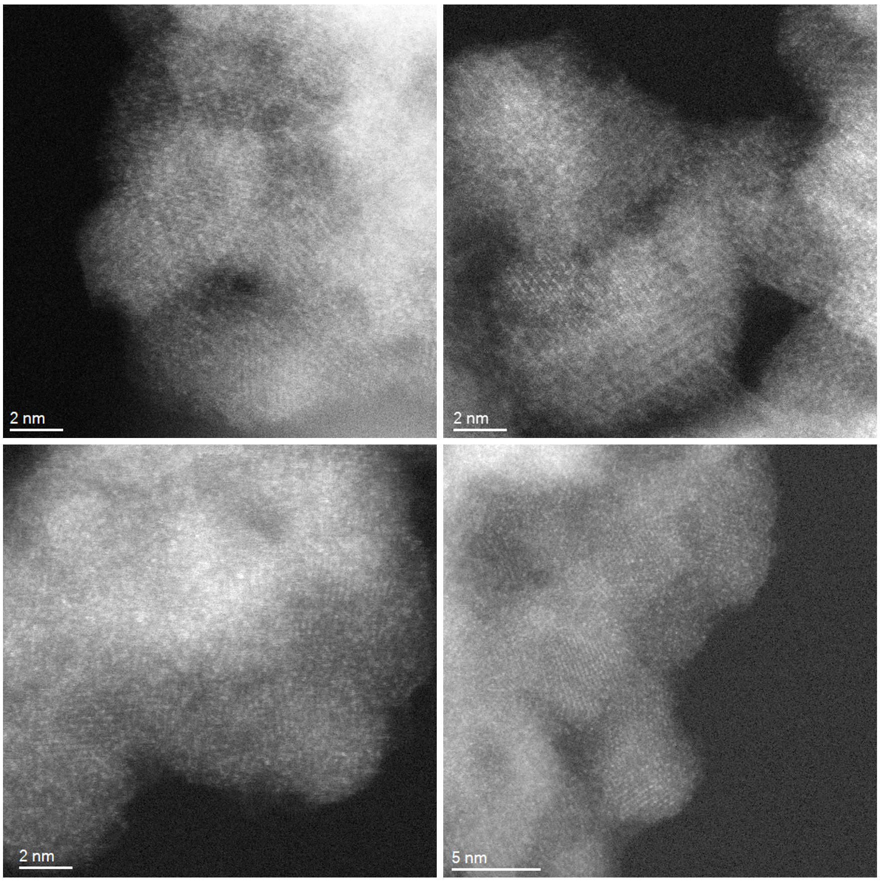

Figure S4. HAADF images of $(Ga,Al)_2O_{3(1:3)}$ showing disordered agglomerated particles in $(Ga,Al)_2O_{3(1:3)}$ (top) and $(Ga,Al)_2O_{3(1:6)}$ (bottom).

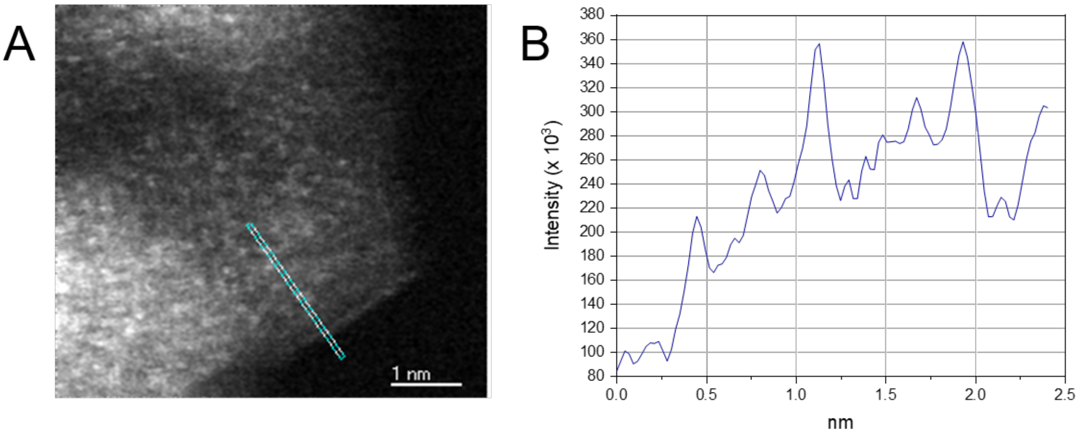

Figure S5. HAADF image of $(Ga,Al)_2O_{3(1:3)}$ (A), and intensity line profile of a particle edge (B).

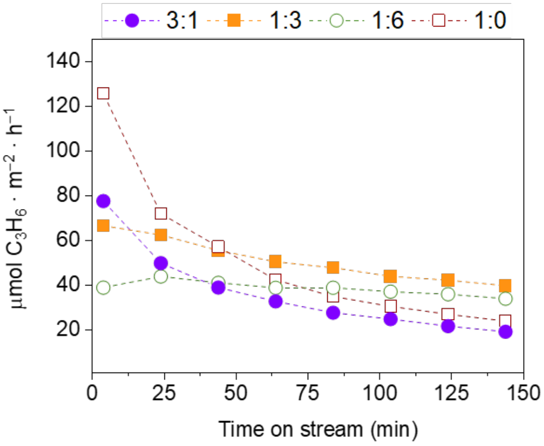

Figure S6. Surface-area normalized activity of $(Ga,Al)_2O_3$ catalysts.

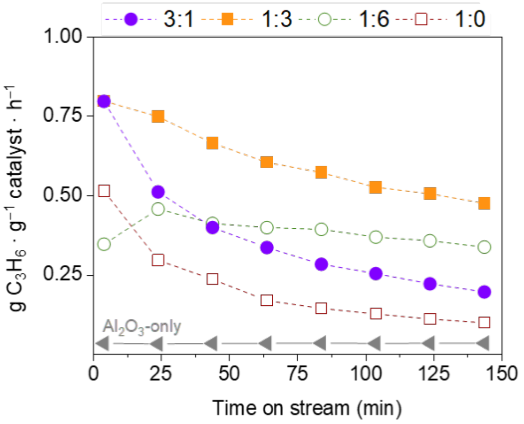

Figure S7. Productivity in PDH of $(Ga,Al)_2O_3$ catalysts along with the reference material γ-Al_2O_3.

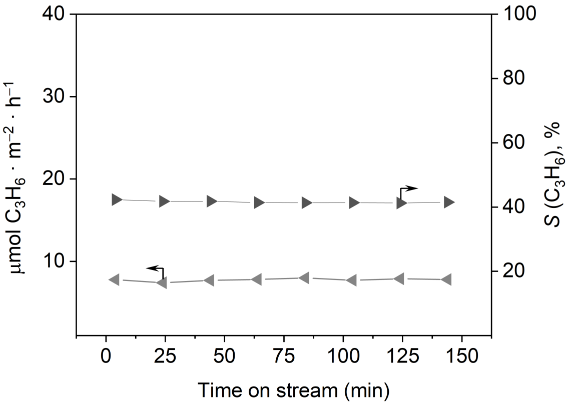

Figure S8. Surface area-normalized PDH activity and propene selectivity of γ-Al_2O_3.

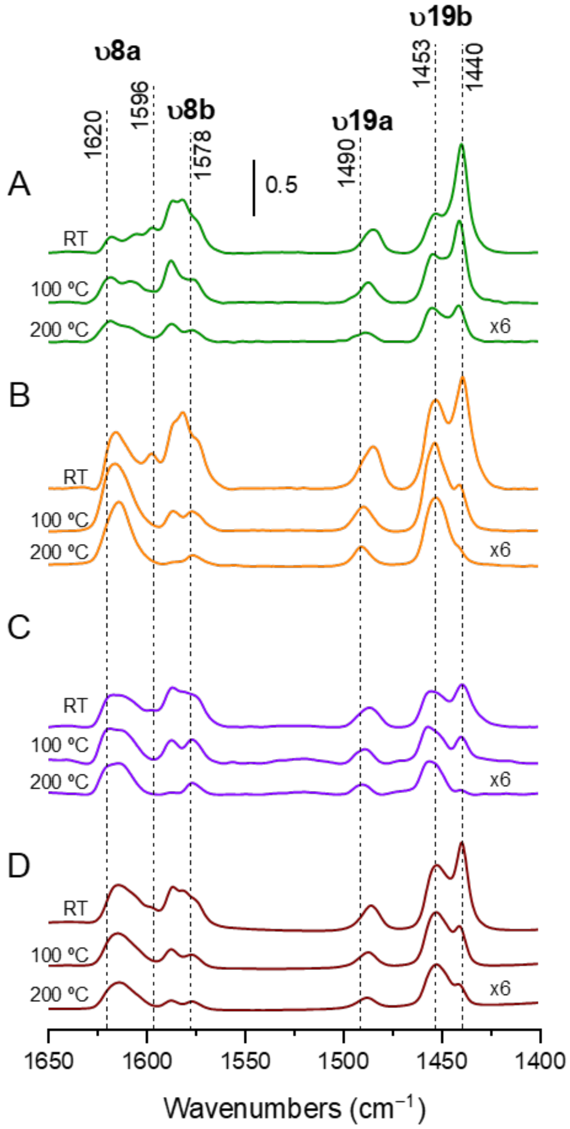

Figure S9. Transmission Py-FTIR spectra for $(Ga,Al)_2O_{3(1:6)}$ (A), $(Ga,Al)_2O_{3(1:3)}$ (B), $(Ga,Al)_2O_{3(3:1)}$ (C), $(Ga,Al)_2O_{3(1:0)}$ (D).

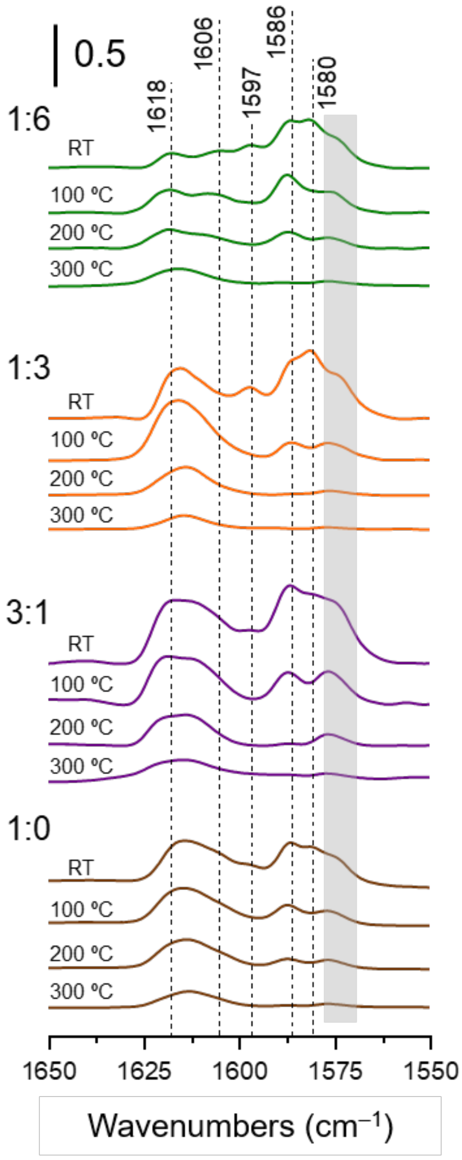

Figure S10. Transmission Py-FTIR spectra in the 1650-1525 cm^{-1} region for $(Ga,Al)_2O_3$ catalysts after evacuation (10^{-5} mbar) at the indicated temperatures. Shaded areas indicate bands corresponding to physisorbed pyridine.

Py-FTIR. Main bands corresponding to Py bonded to Lewis acid sites (LAS) can be found at ca. 1630-1600, 1490 and 1450 cm^{-1} (υ8a, υ19a and υ19b vibration modes in the Wilson notation, Table S7).[15,16] Within the range between ca. 1630 and 1600 cm^{-1}, Py bands with higher wavenumbers indicate a stronger Lewis acid character.[17] Pyridine protonated by strong Brønsted acid sites (BAS) gives bands at 1635-1640 and 1545 cm^{-1}. Py on LAS, mild/weak BAS (i.e., H-bonded Py) and strong BAS features a band at 1490 cm^{-1}; this overlap of bands complicates their assignment.[15,18,19] Weak/mild BAS can be identified by bands at ca. 1590 and 1445 cm^{-1}. Bands at ca. 1580 and 1440 cm^{-1} can be due to physisorbed pyridine, H-bonded pyridine or, in some cases, Py on LAS.[20,21]

Figure S9 shows the Py-FTIR spectra of $(Ga,Al)_2O_3$ catalysts within the region of interest (1650-1400 cm^{-1}). Py desorbed from $(Ga,Al)_2O_{3(1:6)}$ at room temperature leaves only low intensity LAS bands between 1625-1610 cm^{-1}, with the main band centered at 1618 cm^{-1}. The intensity of the

LAS bands for $(Ga,Al)_2O_{3(1:6)}$ in this region does not change notably when increasing the Py desorption temperature (T_{des}) up to 300 ºC, consistent with strong LAS (Figure S10). In contrast, bands at lower wavenumbers, i.e. at ca. 1606 and 1597 cm^{-1}, are likely due to Py on weak LAS and their intensities decrease with increasing T_{des}, until the disappearance of these bands at 300 ºC. Interestingly, the band centered at 1597 cm^{-1} is also pronounced in $(Ga,Al)_2O_{3(1:3)}$ and is less intense and less well-defined in Ga-rich $(Ga,Al)_2O_{3(3:1)}$ and $(Ga,Al)_2O_{3(1:0)}$. LAS bands between 1625-1610 cm^{-1} are more intense, especially at lower T_{des} (i.e., RT-200 ºC), in $(Ga,Al)_2O_{3(1:3)}$, $(Ga,Al)_2O_{3(3:1)}$ and $(Ga,Al)_2O_{3(1:0)}$ as compared to Al-rich $(Ga,Al)_2O_{3(1:6)}$ (Figure S10).

Before presenting the results of Py adsorption onto BAS in $(Ga,Al)_2O_3$ materials, we discuss the OH region of the calcined $(Ga,Al)_2O_3$ NPs after their evacuation at 100 °C-300 °C (Figure S11). The main bands seen in $(Ga,Al)_2O_{3(1:0)}$ are a relatively sharp band at ca. 3621 cm^{-1} and a broad band at ca. 3456 cm^{-1}, in addition to a low intensity band at ca. 3744 cm^{-1}. The latter band appears at this position for all four $(Ga,Al)_2O_3$ NPs, although its intensity decreases with increasing Al content. In contrast, a blue shift of the 3621 and 3456 cm^{-1} bands in $(Ga,Al)_2O_{3(1:0)}$ is observed when increasing amounts of Al are incorporated, i.e. these bands appear at ca. 3657 and 3515 cm^{-1} in $(Ga,Al)_2O_{3(3:1)}$ and at ca. 3669 and 3536 cm^{-1} in $(Ga,Al)_2O_{3(1:3)}$ and in $(Ga,Al)_2O_{3(1:6)}$; the band at 3515 cm^{-1} and 3536 cm^{-1} also broadens (Figure S11). No notable band shifts or intensity changes are observed after evacuation at higher temperatures (up to 300 °C), besides a subtle shoulder that emerges for $(Ga,Al)_2O_3$ NPs at ca. 3354 cm^{-1}. Previous report ascribed the band at ca. 3669 cm^{-1} to Ga–OH–Al bridging hydroxyls.[22] Overall, the incorporation of Al into $(Ga,Al)_2O_3$ NPs induces a blue shift of two major OH bands, indicative of their increased Brønsted acidity.

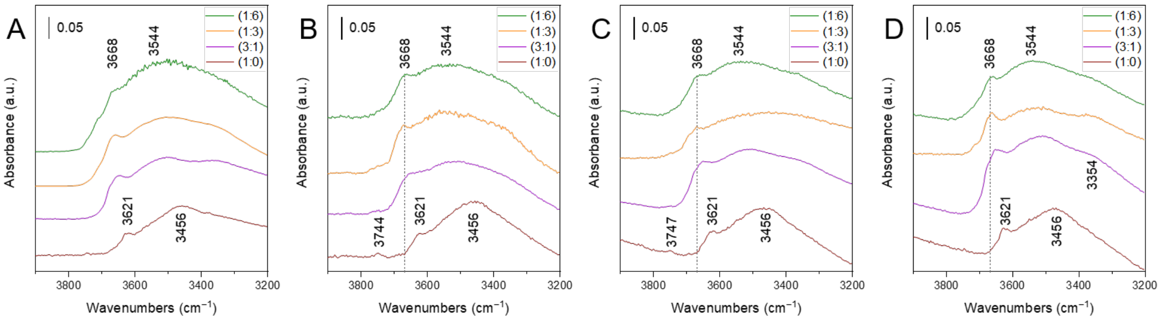

Figure S11. Transmission Py-FTIR spectra of the hydroxyl region in dehydroxylated $(Ga,Al)_2O_3$ catalysts before (A), and after Py adsorption and subsequent evacuation at 100 ºC (B), 200 °C (C), and 300 °C (D). Py adsorbed on weak/mild BAS (H-bonded pyridine), identified by bands at ca. 1586 and 1580 cm^{-1}, is found in all prepared materials. The band at 1586 cm^{-1} is more intense in Ga-rich $(Ga,Al)_2O_{3(1:0)}$ and $(Ga,Al)_2O_{3(3:1)}$, whereas the band at 1580 cm^{-1} is more intense in Al-rich $(Ga,Al)_2O_{3(1:6)}$ and $(Ga,Al)_2O_{3(1:3)}$ (Figure S10). The band at 1580 cm^{-1} disappears at T_{des} = 100 °C, however, the band at 1586 cm^{-1} is found at T_{des} = 200 °C for $(Ga,Al)_2O_{3(1:0)}$ and $(Ga,Al)_2O_{3(1:6)}$. No strong BAS sites were found on the calcined $(Ga,Al)_2O_3$ NPs.

To further assess the presence of strong BAS and validate the distribution of LAS, the 2,6-dimethylpyridine (2,6-DMPY) probe molecule was used (Figure S12).[21] No clear bands corresponding to strong BAS (i.e. bands in the region 1640-1655, 1630, 1473 or 1415 cm^{-1}) are observed. However, the prepared materials feature bands due to 2,6-DMPY bonded to LAS in the range 1620-1595 cm^{-1}. 2,6-DMPY is more easily desorbed in Al-containing catalysts in contrast to

$(Ga,Al)_2O_{3(1:0)}$, also indicating the presence of a higher relative fraction of weaker LAS in Al-containing materials (Figure S12, shaded areas). In the supported materials, the high dispersion of $(Ga,Al)_2O_3$ on the SiO_2 support hinders the detection of bands due to 2,6-DMPY on LAS.

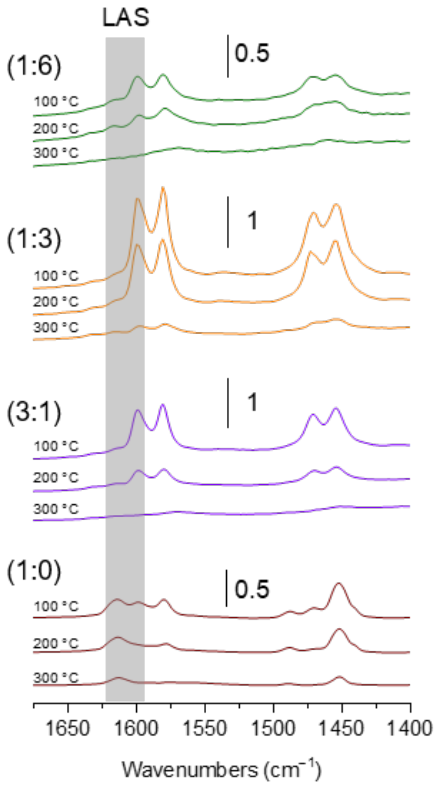

Figure S12. Transmission 2,6-DMPY-FTIR spectra after evacuation at 100-300 °C (10^{-5} mbar) for $(Ga,Al)_2O_3$ catalysts. The shaded region (1595-1620 cm^{-1}) indicates the position of bands owing to 2,6-DMPY on LAS.

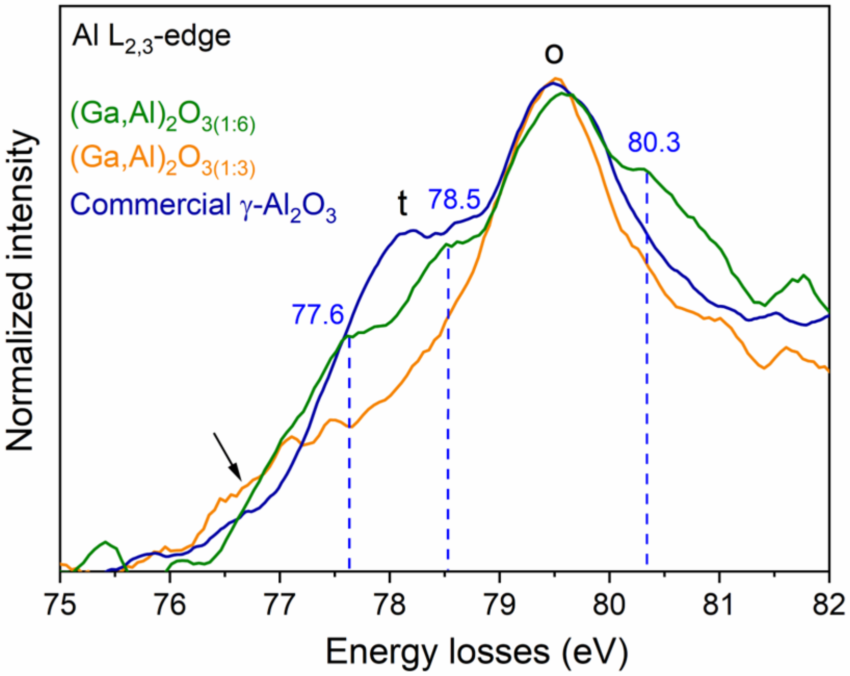

Figure S13. EELS plot comparing energies at the Al $L_{2,3}$-edge between the $(Ga,Al)_2O_{3(1:3)}$, $(Ga,Al)_2O_{3(1:6)}$, and the reference γ-Al_2O_3 (orange, green and blue traces, respectively).

Electron energy loss spectroscopy (EELS) of the Al $L_{2,3}$-edge allowed to assess the density of unoccupied states associated with Al atoms in tetrahedral and octahedral positions (Al_{tetra} and Al_{oct}, respectively) in $(Ga,Al)_2O_{3(1:3)}$ and $(Ga,Al)_2O_{3(1:6)}$ and to compare it to a γ-Al_2O_3 reference (Figure S13). The density of unoccupied states associated to Al_{tetra} sites (marked with "t") drops substantially in $(Ga,Al)_2O_{3(1:3)}$, in comparison with the γ-Al_2O_3 reference material. In addition, we observe a shift of this feature towards lower energy losses, indicating a net charge transfer from Ga to Al_{tetra}. The EELS spectrum of the $(Ga,Al)_2O_{3(1:6)}$ shows a higher intensity of the feature associated with Al_{tetra} sites. However, a splitting of the signal into two peaks at 77.6 and 78.5 eV and the appearance of a new feature at 80.3 eV in the Al_{oct} region (> 79 eV) indicate a pronounced crystal field splitting for this material. Given that atomic-resolution ADF-STEM images showed a similar degree of structural disorder for both $(Ga,Al)_2O_{3(1:3)}$ and $(Ga,Al)_2O_{3(1:6)}$ (Figure S4), the observed crystal field splitting can be associated with the presence of a relatively larger portion of pentacoordinated Al sites, as detected by NMR.

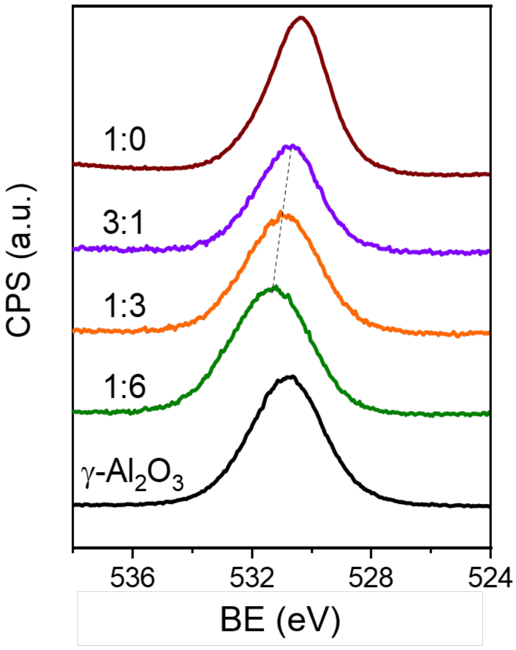

Figure S14. XPS O 1s plots of $(Ga,Al)_2O_3$ NPs and the γ-Al_2O_3 reference.

XPS analysis was performed to evaluate the electronic states of oxygen atoms in the prepared $(Ga,Al)_2O_3$ materials. We observe that the binding energy (BE) of the O 1s peak increases gradually, from 529.9 eV in $(Ga,Al)_2O_{3(1:0)}$ to 530.6 eV and 530.9 eV in $(Ga,Al)_2O_{3(3:1)}$ and $(Ga,Al)_2O_{3(1:3)}$ reaching 531.3 eV in $(Ga,Al)_2O_{3(1:6)}$ (Figure S14). This shift indicates a decreasing electron density on the oxygen atom with increasing Al content in $(Ga,Al)_2O_3$ NPs, which is counterintuitive, as it suggests more ionic Ga–O bonds (and higher oxygen hardness and basicity) relative to Al–O bonds, despite the lower electronegativity of Al relative to Ga (1.61 and 1.81, respectively).[23]

Tables

Table S1. Results of N_2 physisorption, ICP-OES and XRD (crystallite size) analyses.

Entry	Material	S_{BET} (m^2 g^{-1})	BJH pore diameter (nm)	BJH pore volume (ml g^{-1})	ICP (wt%)		Atomic Ga/Al ratio by ICP-OES	Average crystallite size (nm) *
					Ga	Al		
1	$(Ga,Al)_2O_{3(1:0)}$	98	2.5	0.2	71.0	–	–	5.3
2	$(Ga,Al)_2O_{3(3:1)}$	245	3.8	0.3	58.8	11.4	2:1	2.4
3	$(Ga,Al)_2O_{3(1:3)}$	286	6.6	0.7	29.5	22.6	1:2	2.7
4	$(Ga,Al)_2O_{3(1:6)}$	270	5.7	0.6	16.8	36.5	1:5.6	2.8

* Calculated using the Scherrer equation.[24]

Table S2. Results of EXAFS fittings of $(Ga,Al)_2O_3$ materials.

Entry	Material	Path #	Path	N	Distance (Å)	σ^2 ($Å^2$)	R-factor
1	Ga-Al(1:0)	1	Ga–O	5.7(8)	1.91(1)	0.012(2)	0.011
		2	Ga–Ga1	3.0(6)	3.00(1)	0.010*	
		3	Ga–Ga2	3.3(8)	3.37(2)	0.010*	
2	Ga-Al(3:1)	1	Ga–O	5.2(5)	1.89(1)	0.010(1)	0.008
		2	Ga–(Ga, Al)1	3.8(9)	3.01(2)	0.015*	
		3	Ga–(Ga, Al)2	4.2(9)	3.37(2)	0.015*	
3	Ga-Al(1:3)	1	Ga–O	4.0(2)	1.86(1)	0.006(1)	0.004
		2	Ga–(Ga, Al)1	3.1(6)	3.01(2)	0.015*	
		3	Ga–(Ga, Al)2	6.6(9)	3.43(1)	0.015*	
4	Ga-Al(1:6)	1	Ga–O	4.0(2)	1.84(1)	0.005(1)	0.005
		2	Ga–(Ga, Al)1	3.9(7)	3.00(1)	0.015*	
		3	Ga–(Ga, Al)2	7.4(9)	3.42(1)	0.015*	

*Fixed values

Table S3. Relative abundances of coordination sites (%), chemical shifts (in ppm) and quadrupolar coupling (in MHz) obtained from Czjzek fittings of ^{71}Ga MAS NMR data (plots in Figure S3).

Entry	Material	^{71}Ga							
		Ga$_{IV}$				Ga$_{VI}$			
		%	$\bar{\delta}_{iso}$	$\Delta\bar{\delta}_{iso}$	$\bar{C}_Q$	%	$\bar{\delta}_{iso}$	$\Delta\bar{\delta}_{iso}$	$\bar{C}_Q$
1	$(Ga,Al)_2O_{3(3:1)}$	57	194.	47.6	14.1	43	57.1	36.2	10.5
2	$(Ga,Al)_2O_{3(1:3)}$	72	192.	49.2	13.6	28	55.1	33.9	11.4
3	$(Ga,Al)_2O_{3(1:6)}$	86	190.	53.6	15.4	14	48.0	46.0	11.5

Table S4. Relative abundances of coordination sites (%), chemical shifts (in ppm) and quadrupolar coupling (in MHz) obtained from Czjzek fittings of ^{27}Al MAS NMR data (plots in Figure S3).

Entry	Material	^{27}Al											
		Al$_{IV}$				Al$_{V}$				Al$_{VI}$			
		%	$\bar{\delta}_{iso}$	$\Delta\bar{\delta}_{iso}$	$\bar{C}_Q$	%	$\bar{\delta}_{iso}$	$\Delta\bar{\delta}_{iso}$	$\bar{C}_Q$	%	$\bar{\delta}_{iso}$	$\Delta\bar{\delta}_{iso}$	$\bar{C}_Q$
1	$(Ga,Al)_2O_{3(3:1)}$	8	79.2	10.1	8.2	–	–	–	–	92	18.4	6.6	4.9
2	$(Ga,Al)_2O_{3(1:3)}$	12	78.0	9.1	8.1	–	–	–	–	88	16.1	7.6	5.0
3	$(Ga,Al)_2O_{3(1:6)}$	22	77.5	12.2	8.2	12	42.7	11.9	6.9	66	15.3	8.8	5.6

Table S5. Results from catalytic tests and carbon deposition TGA experiments.

Entry	Catalyst	Propane conversion (%)$^{a)}$	Propene selectivity (%)$^{a)}$	Coking (TGA)		
				Weight gain (%)	Per SA (mg$_{coke}$ m^{-2})	Per Ga wt% (mg$_{coke}$ mg Ga^{-1})
1	$(Ga,Al)_2O_{3(1:0)}$	12.4 (4.6)	87 (62)	5.1	51.9	0.07
2	$(Ga,Al)_2O_{3(3:1)}$	29.0 (6.6)	76 (68)	7.6	31.1	0.13
3	$(Ga,Al)_2O_{3(1:3)}$	26.3 (7.8)	86 (90)	6.3	21.9	0.21
4	$(Ga,Al)_2O_{3(1:6)}$	19.8 (6.5)	85 (85)	1.8	6.6	0.11

a) Data after 4 min and 144 min (in parenthesis), estimated error is ca. ± 2%.

Table S6. Surface area-normalized, Ga-weight normalized PDH activities and productivities of $(Ga,Al)_2O_3$ catalysts.

Entry	Catalyst	Surface area-normalized activity (μmol C_3H_6 m^{-2} h^{-1})[a]	Ga-weight normalized activity (mol C_3H_6 mol Ga^{-1} h^{-1})[a]	Productivity (g C_3H_6 $g_{catalyst}^{-1}$ h^{-1})[a]
1	$(Ga,Al)_2O_{3(1:0)}$	125 (24)	1.21 (0.23)	0.51 (0.10)
2	$(Ga,Al)_2O_{3(3:1)}$	77 (19)	2.25 (0.55)	0.80 (0.19)
3	$(Ga,Al)_2O_{3(1:3)}$	66 (40)	4.48 (2.67)	0.80 (0.47)
4	$(Ga,Al)_2O_{3(1:6)}$	39 (34)	3.41 (3.32)	0.35 (0.34)

[a] Data after 4 min and 144 min (in parenthesis)

Table S7. Characteristic positions of FTIR bands (in cm^{-1}) observed for pyridine adducts on oxide surfaces.[15,16]

Site	Vibrational mode			
	v8a	v8b	v19a	v19b
Lewis	1600-1630	1580w	1490 w	1450, 1456
Brønsted	1640	1610	1490	1545
H-bonded	1595	1580	1490 w	1445
Gas-phase	1584	1578	1483	1439

Weak bands are marked with ‘w’

Table S8. ^{15}N chemical shifts, FWHM and relative areas of Lewis acid sites obtained by Gaussian fittings of CPMAS spectra.

Material	LAS peak (ppm)	FWHM (ppm)	Area (%)	DNP enhancement factor
$(Ga,Al)_2O_{3(1:6)}$	235	12.8	9	104
	242	15.0	7	
	265	24.9	74	
	282	17.1	10	
$(Ga,Al)_2O_{3(1:3)}$	234	11.0	7	84
	241	15.6	15	
	265	23.3	67	
	282	15.9	11	
$(Ga,Al)_2O_{3(3:1)}$	241	15.6	24	110
	266	24.9	67	
	282	14.3	9	
$(Ga,Al)_2O_{3(1:0)}$	240	15.8	23	54
	265	26.4	63	
	281	14.9	14	

Table S9. ^{15}N chemical shifts, FWHM and relative areas of Lewis acid sites obtained by Gaussian fittings of $^{15}N\{^{27}Al\}$ *J*-HMQC NMR spectra.

Material	LAS peak (ppm)	FWHM (ppm)	Area (%)
$(Ga,Al)_2O_{3(1:6)}$	234	8.8	19
	242	9.3	4
	264	22.9	71
	277	11.7	6
$(Ga,Al)_2O_{3(1:3)}$	234	8.4	20
	243	9.3	4
	263	20.0	60
	275	13.1	16
$(Ga,Al)_2O_{3(3:1)}$	234	8.8	7
	264	16.0	65
	277	11.8	28

Table S10. Experimental parameters used in ^{15}N DNP SENS experiments.

Experiment	Experimental parameters
^{15}N{^{1}H} CPMAS	The experiments were performed with ν_{R} = 10 kHz, ν_{RF}(^{1}H) = 100 kHz for 90° pulse, ν_{RF}(^{1}H) = 54 kHz for CP, ν_{RF}(^{15}N) = 32 kHz for CP, τ_{CP} = 4 ms, ν_{RF}(^{1}H) = 100 kHz for SPINAL-64 heteronuclear decoupling, τ_{RD} = 5.6 s ($(\mathrm{Ga,Al})_2\mathrm{O}_{3(1:6)}$), 5.7 s ($(\mathrm{Ga,Al})_2\mathrm{O}_{3(1:3)}$), 5.3 s ($(\mathrm{Ga,Al})_2\mathrm{O}_{3(3:1)}$) and 3.4 s ($(\mathrm{Ga,Al})_2\mathrm{O}_{3(1:0)}$), *ns* = 2048 ($(\mathrm{Ga,Al})_2\mathrm{O}_{3(1:6)}$, $(\mathrm{Ga,Al})_2\mathrm{O}_{3(1:3)}$), 4096 ($(\mathrm{Ga,Al})_2\mathrm{O}_{3(3:1)}$) and 256 ($(\mathrm{Ga,Al})_2\mathrm{O}_{3(1:0)}$), *AT* = 3.2 h ($(\mathrm{Ga,Al})_2\mathrm{O}_{3(1:6)}$, $(\mathrm{Ga,Al})_2\mathrm{O}_{3(1:6)}$), 6.0 h ($(\mathrm{Ga,Al})_2\mathrm{O}_{3(3:1)}$) and 0.2 h ($(\mathrm{Ga,Al})_2\mathrm{O}_{3(1:0)}$).
^{15}N{^{27}Al} *J*-HMQC	The experiments were performed with ν_{R} = 10 kHz, ν_{RF}(^{1}H) = 100 kHz for 90° pulse, ν_{RF}(^{1}H) = 100 kHz for CP, ν_{RF}(^{15}N) = 100 kHz for CP, τ_{CP} = 4 ms, ν_{RF}(^{27}Al) = 23 kHz for 90° pulse, ν_{RF}(^{15}N) = 50 kHz for 180° pulse, ν_{RF}(^{1}H) = 100 kHz for SPINAL-64 heteronuclear decoupling, τ_{RD} = 5.6 s ($(\mathrm{Ga,Al})_2\mathrm{O}_{3(1:6)}$), 5.7 s ($(\mathrm{Ga,Al})_2\mathrm{O}_{3(1:3)}$) and 5.3 s ($(\mathrm{Ga,Al})_2\mathrm{O}_{3(3:1)}$), *ns* = 4096 ($(\mathrm{Ga,Al})_2\mathrm{O}_{3(1:6)}$, $(\mathrm{Ga,Al})_2\mathrm{O}_{3(1:3)}$) and 8192 ($(\mathrm{Ga,Al})_2\mathrm{O}_{3(3:1)}$), *AT* = 6.4 h ($(\mathrm{Ga,Al})_2\mathrm{O}_{3(1:6)}$), 6.5 h ($(\mathrm{Ga,Al})_2\mathrm{O}_{3(1:6)}$)) and 12.1 h ($(\mathrm{Ga,Al})_2\mathrm{O}_{3(3:1)}$).
^{15}N{^{71}Ga} *J*-HMQC	The experiments were performed ν_{R} = 10 kHz, ν_{RF}(^{1}H) = 50 kHz for 90° pulse and SPINAL-64 heteronuclear decoupling, ν_{RF}(^{1}H) = 46 kHz for CP, ν_{RF}(^{15}N) = 23 kHz for CP and 180° pulse, τ_{CP} = 4.5 ms, ν_{RF}(^{71}Ga) = 31 kHz for 90° pulse, τ_{RD} = 3.2 s, *ns* = 49152, *AT* = 43.7 h.

Equations

Propane conversion (%):

$$X = \frac{Flow_{In} C_3H_8 - Flow_{Out} C_3H_8}{Flow_{In} C_3H_8} \cdot 100$$

Where:

$Flow_{In}$ C_3H_8 *= inlet flow of propane (mol · h^{-1})*

$Flow_{Out}$ C_3H_8 *= outlet flow of propane (mol · h^{-1})*

Propene formation rate (Ga-normalized) (*mol · mol* $_{Ga}^{-1}$ · h^{-1}):

$$r_{C3H6} = \frac{Flow_{Out} C_3H_6}{\mathrm{Mol\ (Ga)} \cdot h}$$

Where:

$Flow_{Out}$ C_3H_6 *= outlet flow of propene (mol · h^{-1})*

Selectivity to propene ($\%_{C3H6}$):

$$S = \frac{Flow_{Out} C_3H_6}{\Sigma Flow_{Out}} \cdot 100$$

Where:

$Flow_{Out}$ C_3H_6 *= outlet flow of propene (mol · h^{-1})*

$\sum$ $Flow_{Out}$ *= outlet flow of all carbon products (mol · h^{-1})*

References

1 T. Wang, S. S. Farvid, M. Abulikemu and P. V Radovanovic, *J. Am. Chem. Soc.*, 2010, **132**, 9250–9252.

2 B. D. . Cullity and S. R. Stock, *Elements of X-ray Diffraction*, Prentice-Hall, 2001.

3 W. Van Beek, O. V. Safonova, G. Wiker and H. Emerich, *Phase Transitions*, 2011, **84**, 726–732.

4 C. S. S. R. Kumar, *X-ray and Neutron Techniques for Nanomaterials Characterization*, Springer Nature, Berlin, 2016.

5 B. Ravel and M. Newville, *J. Synchrotron Radiat.*, 2005, **12**, 537–541.

6 J. Åhman, G. Svensson and J. Albertsson, *Acta Crystallogr. Sect. C Cryst. Struct. Commun.*, 1996, **52**, 1336–1338.

7 D. Massiot, F. Fayon, M. Capron, I. King, S. Le Calvé, G. Hoatson, I. King, B. Alonso, J.-O. Durand, B. Bujoli, Z. Gan and G. Hoatson, *Magn. Reson. Chem.*, 2002, **40**, 70–76.

8 J. B. d’Espinose de Lacaillerie, C. Fretigny and D. Massiot, *J. Magn. Reson.*, 2008, **192**, 244–251.

9 D. A. Shirley, *Phys. Rev. B*, 1972, **5**, 4709–4714.

10 S. Brunauer, P. H. Emmett and E. Teller, *J. Am. Chem. Soc.*, 1938, **60**, 309–319.

11 E. P. Barrett, L. G. Joyner and P. P. Halenda, *J. Am. Chem. Soc.*, 1951, **73**, 373–380.

12 C. A. Schneider, W. S. Rasband and K. W. Eliceiri, *Nat. Methods*, 2012, **9**, 671–675.

13 M. Zinkevich, F. M. Morales, H. Nitsche, M. Ahrens, M. Rühle and F. Aldinger, *Z. Met.*, 2004, **95**, 756–762.

14 Ľ. Smrčok, V. Langer and J. Křesťan, *Acta Crystallogr. Sect. C Cryst. Struct. Commun.*, 2006, **62**, i83–i84.

15 B. A. Morrow and I. A. Cody, *J. Phys. Chem.*, 1976, **80**, 1995–1998.

16 S. D. Jackson and J. S. J. Hargreaves, *Metal Oxide Catalysis*, WILEY-VCH Verlag GmbH & Co. KGaA, Weinheim, 2009.

17 M. I. Zaki, M. A. Hasan, F. A. Al-Sagheer and L. Pasupulety, *Colloids Surfaces A Physicochem. Eng. Asp.*, 2001, **190**, 261–274.

18 W. R. Gunther, V. K. Michaelis, R. G. Griffin and Y. Roman-Leshkov, *J. Phys. Chem. C*, 2016, **120**, 28533–28544.

19 M. S. Solum, K. L. Altmann, M. Strohmeier, D. A. Berges, Y. Zhang, J. C. Facelli, R. J. Pugmire and D. M. Grant, *J. Am. Chem. Soc.*, 1997, **119**, 9804–9809.

20 J. C. Lavalley, M. Daturi, V. Montouillout, G. Clet, C. Otero Areán, M. Rodríguez Delgado and A. Sahibed-dine, *Phys. Chem. Chem. Phys.*, 2003, **5**, 1301–1305.

21 F. Thibault-Staruk and M. Francoise, *Characterization of Solid Materials and Heterogeneous Catalysts: From Structure to Surface Reactivity*, Wiley-VCH Verlag GmbH & Co. KGaA, First., 2012.

22 Y. N. Pushkar, A. Sinitsky, O. O. Parenago, A. N. Kharlanov and E. V. Lunina, *Appl. Surf. Sci.*, 2000, **167**, 69–78.

23 L. Pauling, 1932, **54**, 3570–3582.

24 P. Scherrer and P. Debye, *Nachr. Ges. Wiss. Göttingen, Math.-physik. Klasse*, 1918, **2**, 101–120.